



Comparison between shadow imaging and in-line holography for measuring droplet size distributions

Martin A. Erinin^{1,2} · Baptiste Néel¹ · Megan T. Mazzatenta¹ · James H. Duncan² · Luc Deike^{1,3}

Received: 28 November 2022 / Revised: 6 April 2023 / Accepted: 9 April 2023 / Published online: 4 May 2023
© The Author(s) 2023

Abstract

A direct comparison of the droplet size and number measurements using in-line holography and shadow imaging is presented in three dynamically evolving laboratory scale experiments. The two experimental techniques and image processing algorithms used to measure droplet number and radii are described in detail. Droplet radii as low as $r = 14 \mu\text{m}$ are measured using in-line holography and $r = 50 \mu\text{m}$ using shadow imaging. The droplet radius measurement error is estimated using a calibration target (reticle) and it was found that the holographic technique is able to measure droplet radii more accurately than shadow imaging for droplets with $r \leq 625 \mu\text{m}$. Using the measurements of droplet number and size we quantitatively cross-validate and assess the accuracy of the two measurement techniques. The droplet size distributions, $N(r)$, are measured in all three experiments and are found to agree well between the two measurement techniques. In one of the laboratory experiments, simultaneous measurements of droplets ($r \geq 14 \mu\text{m}$, using holography) and dry aerosols ($0.07 \lesssim r \lesssim 2 \mu\text{m}$, using a scanning mobility particle sizer and $0.15 \lesssim r \lesssim 5 \mu\text{m}$ using an optical particle sizer) are reported, one of the first such comparison to the best of our knowledge. The total number and volume of droplets is found to agree well between both techniques in the three experiments. We demonstrate that a relatively simple shadow imaging technique can be just as reliable when compared to a more sophisticated holographic measurement technique over their common droplet radius measurement range. The agreement in results is shown to be valid over a large range of droplet concentrations, which include experiments with relatively sparse droplet concentrations as low as 0.02 droplets per image. Advantages and disadvantages for the two techniques are discussed in the context of our results. The main advantages to in-line holography are the greater accuracy in droplet radius measurement, greater spatial resolution, larger depth of field, and the high repetition rate and short pulse duration of the laser light source. In comparison, the main advantages to shadow imaging are the simpler experimental setup, image processing algorithm, and fewer computer resources necessary for image processing. Droplet statistics like number and size are found to be very reliable between the two methods for large range of droplet densities, $\mathcal{P}_{r>50}$, ranging from $10^{-4} \leq \mathcal{P}_{r>50} \leq 10^{-1} \text{cm}^{-3}$, when the two techniques are implemented as shown in this paper.

1 Introduction

Measurements of droplet statistics in turbulent multiphase flows are important in a wide range of applications, including sea spray and atmospheric sciences (Veron 2015; de Leeuw et al. 2011), soot measurements in internal combustion engines (Hayashi et al. 2011), particle sedimentation (McEwan et al. 2000), and multiphase transport in pipe flow (Sanchis et al. 2011; Boulesteix 2010). Droplet statistics like number, size, speed, and acceleration can be critical to understanding the physics of complex multiphase flows. A large number of intrusive and non-intrusive techniques have been developed to measure droplet statistics, see for example the reviews by Tropea (2011) and Poelma (2020).

✉ Martin A. Erinin
merinin@princeton.edu

✉ Luc Deike
ldeike@princeton.edu

¹ Department of Mechanical and Aerospace Engineering, Princeton University, Princeton, NJ, USA

² Department of Mechanical Engineering, University of Maryland, College Park, MD, USA

³ High Meadows Environmental Institute, Princeton University, Princeton, NJ, USA

Two popular non-intrusive droplet imaging techniques include shadow imaging, see for example Bongiovanni et al. (1997, 2000), and holography, see review by Katz and Sheng (2010). Shadow imaging is widely used because of the simple experimental setup and image processing. The setup uses a camera, a lens, and a diffuse light source to record images of droplets. The diffuse light source is used as backlighting to image the shadows generated by droplets, bubbles, or particles using the camera and lens. The technique has been extensively used to measure the size of droplets and bubbles in multiphase flows, see for example Veron et al. (2012); Troitskaya et al. (2018); Néel and Deike (2022). The principles of shadow imaging can be used with multiple cameras to track the 3D positions and trajectories of particles in multiphase flows, see for example Machicoane et al. (2019); Ruth et al. (2022); Ramírez de la Torre and Jensen (2023); Baker and DiBenedetto (2023). Some of the major sources of uncertainty associated with shadow imaging are related to parallax, correcting for out of focus droplets, and the size dependence of the depth of field, for example, see Geißler and Jähne (1995), Bongiovanni et al. (1997), Kashdan et al. (2003), Warncke et al. (2017), and Barnkob and Rossi (2020). Parallax can be corrected by using a telecentric lens, which preserves magnification across the depth of field or a calibration process. Correcting for out of focus droplets and the size dependence of the depth of field can be achieved via a calibration process. Additionally, some methods can be used to increase the depth of field by using a calibration and post-processing of out of focus droplets, see for example Zhou et al. (2020a). The use of glare points is an additional method used to directly image transparent particles (i.e. droplets and bubbles) with the use of backlighting, see Van de Hulst and Wang (1991) for more details.

In-line holography can be used to measure the size, speed, and acceleration of droplets, see for example, Li et al. (2017); Erinin et al. (2019); Erinin (2020); Erinin et al. (2022). The technique uses a coherent and collimated light source to record holograms of droplets. The images of the holograms contain interference patterns formed by light diffracted at the boundaries of the droplet. The interference patterns contain three-dimensional information about the droplets. Using digital image processing algorithms, the holograms of droplets can be reconstructed to their focal plane, after which the droplet size and location can be measured. In the method proposed in this paper, droplets are reconstructed to their focal plane using edge features, however, it should be noted that many different methods exist for determining the plane of best focus, see for example Khanam et al. (2011), Pan and Meng (2003), and Soontaranon et al. (2008). Because it uses a collimated laser beam, in-line holography does not suffer from

the effects of parallax. Additionally, because of the large depth of field, in the experiments presented in this paper, in-line holography does not require a calibration process to correct for the size-dependent depth of field. Other non-intrusive techniques used to measure droplet size include Phase Doppler Anemometry (PDA) and interferometric laser imaging for droplet sizing (ILIDS) (Tropea 2011).

Measuring the shape of the droplet radius distribution and the total number of droplets in turbulent environments has proven to be challenging in some flow conditions. For example, the density of droplets ejected in a wind-wave tunnel at moderate to high wind speed has been shown to be uncertain, see Fig. 6 in Veron (2015) where the size-dependent sea spray generation function can span several orders of magnitude in the vertical direction. Similarly, the global production of sea salt has also been shown to be uncertain up to a factor as high as 50, see for example Deike et al. (2022). Some of these challenges may be related to the techniques used to measure droplet radii and number. The advantages and disadvantages to holography and shadow imaging have been well documented, see for example, the review by Tropea (2011) or papers specific to each measurement technique like Zhou et al. (2020a) and Guildenbecher et al. (2013). Many previous papers have improved on the limitations of holography or shadow measurements, see for example Guildenbecher et al. (2017), Zhou et al. (2020b), Kamiya et al. (2022), and Ade et al. (2023). While some previous studies have compared the droplet size measurements between shadow and holographic techniques, see for example Guildenbecher et al. (2014), few have conducted a systematic and detailed comparison of the two techniques, with the specific goal of evaluating their respective advantages and disadvantages.

In this article, a direct comparison between shadow imaging and in-line holography is presented. The image processing and calibration methods for techniques are discussed in detail. The two techniques are deployed simultaneously on three different experimental setups where they are used to measure droplet number and size. The three experiments are dynamically evolving, relatively large in scale, and may represent physical processes present in much larger systems like the ocean. Some of the droplet data from those experiments was already published in Néel et al. (2022) and Erinin et al. (2022). The droplet radius measurement error for each method is estimated using a calibration target. We show that the radius error is lower for the holographic technique for droplets with $r \leq 650 \mu\text{m}$. From these measurements, droplet size distributions are constructed and the trade-offs between the two techniques are assessed. We demonstrate that accurate droplet size distributions and number statistics can be obtained with both techniques over a large range of droplet

concentrations. Finally, we conclude that the holographic system offers specific advantages over the shadow imaging at the cost of a more sophisticated experimental setup and data processing.

2 Droplet measurement techniques

The optical setup and image processing details for the holographic and shadow imaging techniques are discussed in this section. Specifications for the two techniques are summarized and compared in Table 1. Figure 1 shows a typical schematic for the deployment of the two measurement techniques. In Sect. 3 the two techniques are compared in three different experimental setups. Technical specifications like camera and lens type used, which are common across all three experiments, are shown on the top half of Table 1 and the specifications to each experiment, like spatial resolution and measurement volume, are shown on the bottom half of Table 1. A number of factors are considered when choosing the camera, lens, and magnification for the shadow and holographic systems. These design considerations directly impact the spatial resolution and depth of field of the two measurement systems, which in turn control the number of droplets that can be measured (controlled by the measurement volume and depth of field) and the size of droplets (controlled by the spatial resolution). One of the main considerations in experiments that produce sparse droplet concentrations and wide size distributions (like the experiments discussed in this paper) is to ensure that the measurement volume is sufficiently large to measure enough droplets. In this paper, the measurement volume between the two techniques are kept approximately equal, which allowed for robust statistics when measuring droplet number. This is especially important in the three experiments discussed in this paper, which produce relatively low droplet densities (ranging from 0.02 to 14 droplets per image, see Table 2). The approximately similar measurement volumes were achieved by choosing a telecentric lens with a low magnification and pairing it with a camera sensor that had a higher pixel pitch compared to the holographic system. If the design choice of matching the spatial resolution of the two systems was made, it would have resulted in a significantly smaller measurement volume for the shadow system. For example, if the magnification for the shadow technique is doubled, the field of view would decrease by a factor of 4 and the depth of field would likely decrease by an even larger factor. A significantly higher magnification on the shadow imaging system would mean statistical convergence for droplet number would not be comparable between the two techniques.

2.1 In-line holography

Holography is a three-dimensional (3D) imaging technique where interference patterns formed by the interaction of a reference beam and light diffracted at object boundaries are recorded by a camera, see Katz and Sheng (2010) and Schnars et al. (2015) for detailed reviews on the application of holography in the context of fluid mechanics. The measurement technique is used in different optical configurations to measure droplets and bubbles in multi-phase flows, see for example Ling and Katz (2014) and Li et al. (2017). In the present experiments, a form of holography in which the reference beam and the recorded image are parallel, called in-line holography, is used to image droplets generated from a water surface in three different experimental setups. The details of the optical setup and image processing algorithm are discussed in the following sections.

2.1.1 Optical setup

The collimated laser beam is generated using an Nd:YLF laser (CrystalLaser, QL527-200-L) as the illumination source. The laser produces light at 527 nm with an intensity of 80 $\mu\text{J}/\text{pulse}$ and pulse duration of 20–30 ns. The beam is decreased in intensity through the use of a neutral density (ND) filter, is spatially filtered, and collimated and expanded via a 50.8 mm diameter converging achromatic lens with a focal length of 300 mm. Note, the use of an achromatic lens is important to ensure a fully collimated beam. The procedure used to align the spatial filter is explained in Beyersdorf (2014). The collimated laser beam is directed into a long-distance microscope lens (K2 DistaMax, Infinity Photo-Optical Co.) which is attached to a high-speed camera (Phantom VEO4K-990-L). The microscope lens is used in place of a bare sensor because it allows the user to adjust the focusing distance and the magnification of the holographic system. Additionally, the use of the microscope lens allows the user to image all droplets with radius greater than r_{\min} across the full measurement volume, see Sect. 2.1.3 for more details. In the present experiments, the numerical aperture ranges from 0.020 to 0.051. The camera is aligned so that the face of the sensor and the optical axis of the lens is coincident with the collimated laser beam. The laser pulse and camera are synchronized via a pulse generator to take holographic image sequences. Note that a Q-Switched laser is used because the short pulse duration allows the users to image high speed flows, however, it is not typically necessary to perform in-line holographic measurements.

Table 1 A comparison of the technical specification of the holographic and shadow imaging systems as they were deployed in the three different experiments.

Technique	Holography	Shadow imaging		
Lighting	Laser	LED white light		
Camera type	Phantom VEO4K-990-L	Basler acA5472-17um		
Camera resolution (px)	4096 x 2304 (9.4 Mpx)	5496 x 3672 (20.2 Mpx)		
Pixel pitch (μm)	6.75	2.4		
Max. frame rate (Hz)	938	17		
Lens type	Long-distance microscope	Telecentric		
Lens model	K2 DistaMax	Opto-E TC4MHR096-E		
Configuration	Sect. 3.1	Sect. 3.2	Sect. 3.3	All cases
Depth of field (cm)	72	50	89.5	3.9*
Field of view (cm^2)	4.30	0.54	2.09	33.6
Measurement volume (cm^3)	310	27	187	131*
Spatial resolution ($\mu\text{m}/\text{px}$)	6.74	2.39	4.71	12.9
r_{\min} (μm)	27	10	19	50

Results for ‘droplets produced by bursting bubbles in the presence of surfactants’ are presented in Sects. 3.1, 3.2 presents results for ‘droplets produced by bursting bubbles in artificial seawater’, and Sect. 3.3 presents results for ‘droplets produced by breaking wind-forced waves’. The minimum accepted droplet radius measurement, r_{\min} , corresponds to a droplet with radius of 4 pixels. *In the shadow imaging case, the depth of field, and thus the measurement volume, depend on the droplet radius, as discussed in Sect. 2.2.3: the starred values are calculated assuming $r \geq 250 \mu\text{m}$

2.1.2 Droplet detection and focal plane reconstruction

Holograms are recorded using the setup described above and reconstructed using an image processing algorithm. The image processing to determine the location and plane of best focus for droplets in each hologram is done in two steps. The image processing method was developed in-house by M.A.E. while doing his dissertation research at the University of Maryland and is loosely based on the hybrid method proposed by Guildenbecher et al. (2013). The time required to reconstruct a hologram is significantly decreased through the use of a GPU compatible MATLAB reconstruction algorithm, which was provided to us by Professor Joseph Katz from Johns Hopkins University (Li et al. 2017).

The first step of the image processing algorithm is to find the location of all droplets in a hologram and measure their location and approximate radius. The sequence of actions necessary to achieve this are shown for a sample hologram in Fig. 2. Figure 2a shows the hologram as it was recorded by the camera. The intensity distribution of the hologram is homogenized by subtracting the hologram background, which is typically accomplished by calculating a time-series (typically 50 images) averaged hologram and subtracting it from the recorded hologram, as seen in Fig. 2 (b). Note that there are many interference patterns in Fig. 2a, such as droplets or particles on the tank wall, that do not change in time and are removed by the background subtraction. The only pronounced features in (b) are interference patterns which were likely produced by moving droplets. The

background-subtracted hologram is digitally reconstructed every 5 mm in the depth direction (y) and the 3D reconstructed volume is collapsed into a single image containing the minimum intensity at each x - z image location. The resulting hologram is referred to as the collapsed hologram and shown in Fig. 2c. The approximate x - z location of each droplet is measured by thresholding the collapsed hologram, the results are shown in Fig. 2d.

The second step of the image processing algorithm is performed on each droplet detected from the first step and consists of finding the plane of best focus, reconstructing the droplet at that location, and accurately measuring the radius of the droplet. These steps are shown in Fig. 3 for a droplet with $r \approx 14 \mu\text{m}$. First a 200 by 200 pixel window is cropped around each droplet from the recorded hologram and is shown in Fig. 3a. The cropped hologram is reconstructed every 500 μm in the depth direction (y direction). A sharpness criterion, loosely based on the one presented in Equation 8 of Guildenbecher et al. (2013), is calculated at each reconstructed plane. Specifically, sharpness was defined as $\mathcal{S} = \sum_x \sum_z M(x, z) \{ [A(x, z) \otimes S_x]^2 + [A(x, z) \otimes S_z]^2 \} / N$ where \mathcal{S} is the sharpness, $A(x, z)$ is the reconstructed image at each y location, S_x and S_z are the horizontal and vertical Sobel kernels, respectively, $M(x, z)$ is a binary mask that is a disk centered at the location of the droplet with a radius (in pixels) of $r_d = 1.2r_0 + 10$, where r_0 is the radius of the droplet detected in the first step described in the previous paragraph, and N is the total number of pixels in the mask. Fig. 3b shows the sharpness criterion near the plane

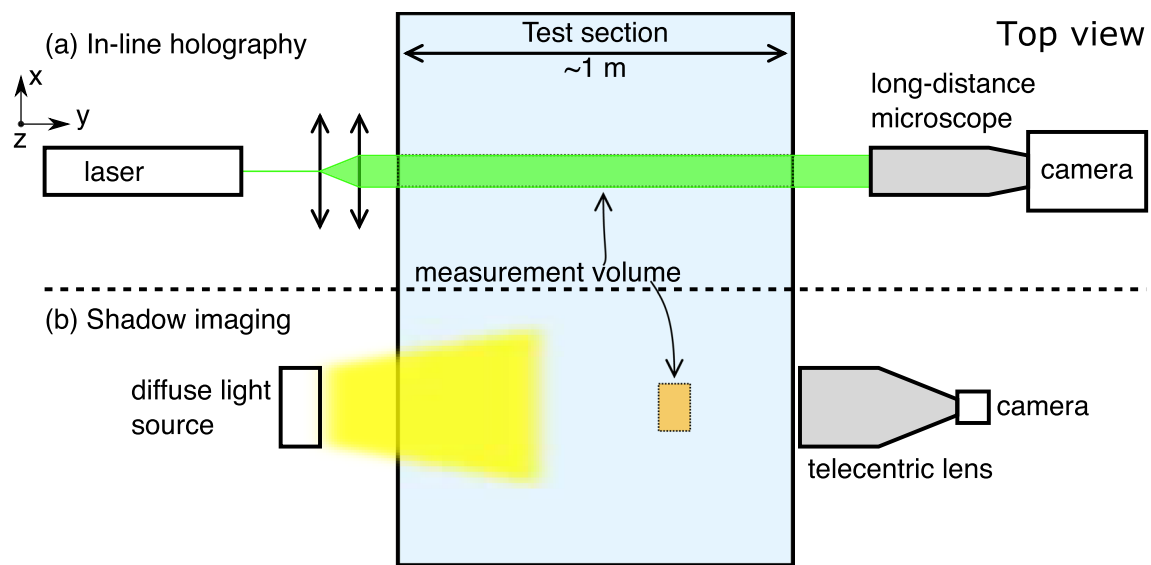


Fig. 1 A schematic showing a typical deployment of the measurement techniques in a test section that is 1 meter wide. The figure represents a top view where the vertical up is in the z -direction and the spanwise is in the y -direction. The top part shows digital in-line holography setup where the illumination light source is provided by a pulsed laser whose beam is spatially filtered, expanded, and collimated to approximately 50 mm in diameter using a series of optical components. The collimated beam is then directed through the measurement region and directly into the long-distance microscope

lens, which is attached to a camera. The lower part shows the shadow imaging setup where the light source is provided by a diffuse light, typically a pulsed LED, which radiates light directly into the telecentric lens and camera, which are positioned on the other side of the tank. The two outlining regions show a typical representation of the depth of the measurement volumes, where in-line holography is typically able to image all droplets inside a measurement volume of $\cong 1$ m in depth. Technical details about the measurement techniques are provided in Table 1

of best focus, where it is maximized. A mean value of an image of the droplet sharpness is calculated at each reconstructed plane and plotted versus the distance from the focal plane ($|y|$), as shown in Fig. 3c. In the case of the sample droplet shown in Fig. 3, the mean sharpness has a peak at $|y| = 1.69$ cm from the lens focal plane. In Fig. 3d, the droplet is reconstructed at this y location and it appears sharp and in focus. The droplet radius is measured from the in focus reconstructed hologram using a gradient-based method described in Sect. 2.3.1.5 in Erinin (2020). This process is repeated for all detected droplets in one image. Typical processing times on an NVIDIA P100 GPU, the GPU used to process the data presented in this paper, are 2.5 seconds to detect the droplets in each image and an additional 2.5 seconds for an accurate radius measurement for each detected droplet.

2.1.3 Calibration and radius error estimates

The in-line holographic system is calibrated using a custom calibration target (from here on referred to as ‘the reticle’), which is used to measure the image spatial resolution, determine minimum measured droplet radius, and estimate the droplet radius measurement error. The reticle is a 25 mm diameter glass slide with 14 chrome sputter deposited circles with radius ranging from $r = 1500$ to 15 μm . The image

spatial resolution is measured by placing the calibration target in the focal plane of the K2 microscope lens, where the circles appear sharp and in focus, see Fig. 4a. The image spatial resolution is calculated by measuring the radius of the circles using the gradient based method described in Erinin (2020). The calibration reticle is also used to determine the minimum measured droplet radius at the two extremes of the measurement volume. The process consists of imaging the calibration target at the two extremes of the measurement volume, the furthest and closest in-tank position from the focal plane of the K2 microscope lens. Then, the hologram of the reticle is reconstructed at the extreme positions so the circles appear in focus. The imaged and reconstructed holograms of the reticle near the tank wall are shown in Fig. 4b and c. Note that all circles in the reconstructed image appears sharp and in focus.

The calibration target is used to assess the maximum expected droplet radius measurement error. In order to achieve this, a hologram of the calibration target is recorded at the furthest distance in the y direction droplets are expected to be measured, a distance of $y = 562$ mm in the case of the experimental setup shown in Fig. 4. At this distance, it is expected that the droplet radius measurement error would be highest for all droplets. The recorded hologram is manually reconstructed so all calibration circles appear in focus. Then, the size of the calibration circles

Table 2 A table comparing the droplet data output of the holographic and shadow imaging systems from the three different experiments

	Holography	Shadow imaging
<i>Droplets produced by bursting bubbles in the presence of surfactants</i>		
# recorded images	1930	3000
Total # droplets	9710	1375
Droplets per image	5.0	0.5
# droplets ($r \geq 50 \mu\text{m}$)	2764	1243
Data set size (GB)	35	0.4 (60 GB stored initially)
Processing time (min)	24	20
<i>Droplets produced by bursting bubbles in artificial seawater</i>		
# recorded images	10764	6000
Total # droplets	151133	24704
Droplets per image	14.0	4.1
# droplets ($r \geq 50 \mu\text{m}$)	46715	24531
Data set size (GB)	140	2.7 (118 GB stored initially)
Processing time (min)	384	45
<i>Droplets produced by breaking wind-forced waves</i>		
# recorded images	86112	84000
Total # droplets	10087	1588
Droplets per image	0.12	0.02
# droplets ($r \geq 50 \mu\text{m}$)	3528	1574
Data set size (GB)	1163	7.9 (1695 GB stored initially)
Processing time (min)	200	145

For each experiment, the total number of recorded images and detected droplets is reported as the sum of the experimental conditions reported for each experimental setup. Processing times for the holographic measurements are reported based on computations done on TigerGPU with 20 P100 NVIDIA GPUs running in parallel. The shadow imaging processing was conducted on a workstation desktop computer. See text for more details

is measured and the radius percent error is calculated as $E_d = 100 \times |r_f - r_i|/r_i$, where E_d is the relative error, r_f is the radius measured from the reconstructed hologram, and r_i is the radius measured from the in focus calibration target. Figure 4a-c show an example of the in focus image of the calibration target in subplot (a), used to measure r_i , and the recorded hologram at the extreme end of the measurement region in subplot (b) and the subsequent reconstruction in (c), which is used to measure r_f . This method is used to obtain a curve of relative error versus droplet radius, which is presented in Fig. 7. The maximum expected measurement error is approximately 1.5 percent. A more detailed discussion on Fig. 7 is presented in Sect. 2.2.3.

2.2 Shadow imaging

The shadow imaging technique is based on the principle that an object placed between a light source and a light-collecting element (*i.e.* a camera sensor) blocks the light transmission, by casting a shadow on the camera sensor. This technique is also sometimes called shadowgraphy, not to be confused

in this case with the technique associated with Schlieren imaging (Settles 2001), or backlighting, then referring solely to the illumination method. Details on the optical setup and image processing required for shadow imaging are discussed in the sections below.

2.2.1 Optical setup

A typical optical setup for shadow imaging is shown in Fig. 1b and consists of the following hardware (see Table 1 for a summary of the details):

- A diffuse (*i.e.* spatially uniform) light source. In the experiments presented in this paper two light sources are used. The first is a LED panel (Phlox LEDW-BL-100x100-HSC-Q-1R-24V, 130,000 cd m⁻² in continuous mode) and the second is a single LED (Veritas mini-Constellation 120 28°, 14,000 lm in continuous mode, 23,800 lm in strobed mode). The Phlox LED panel provided excellent lighting in continuous mode and was used in the ‘droplets produced by bursting bubbles in the presence of surfactants’ experiment (Sect. 3.1) and the ‘drop-

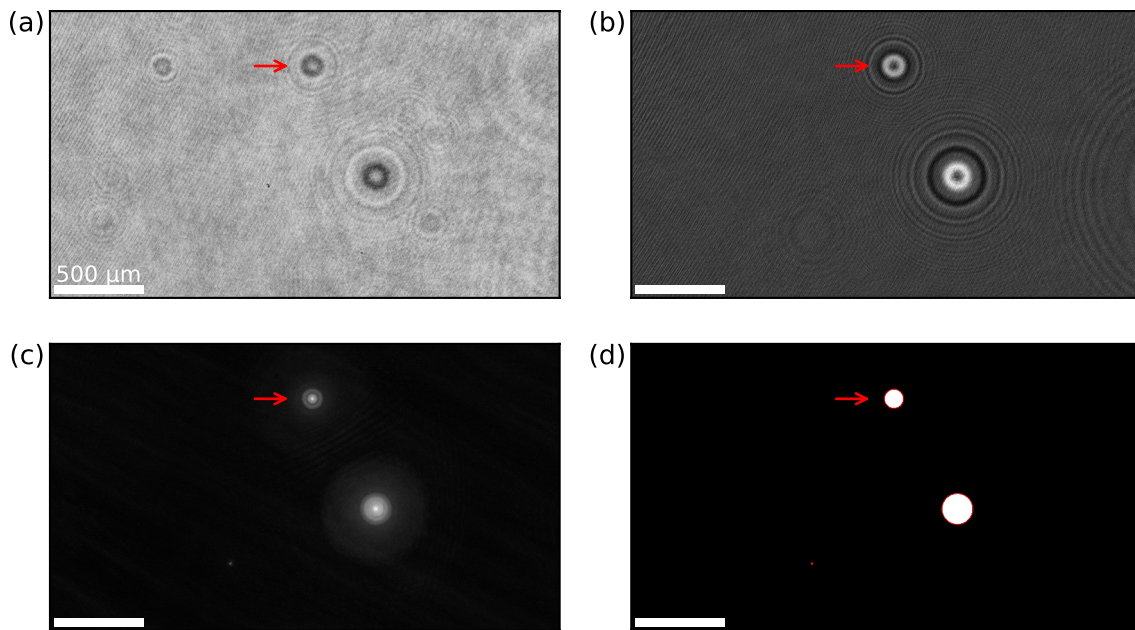


Fig. 2 A sequence of images showing the detection of droplet location and approximate diameter from the recorded holograms. The original recorded hologram is shown in (a). The background subtracted hologram is obtained by subtracting a time-averaged background from (a) and the result is shown in (b). Note that some interference patterns in (a) are dust particles or droplets on the wall whose location does not change with time hence they do not appear in (b).

The background subtracted hologram is reconstructed every 50 μm in depth (y direction) and the resulting 3D reconstructed hologram volume is collapsed in the $x-z$ direction by taking the minimum intensity of each pixel in depth direction y . The collapsed hologram is shown in (c) where drops appear as bright against a black background. The location and approximate size of droplets is measured by thresholding (c), where the result is shown in (d)

lets produced by bursting bubbles in artificial seawater' experiment (Sect. 3.2). The Veritas single LED was used in strobed mode in the 'droplets produced by breaking wind-forced waves' experiments (Sect. 3.3) because droplets moved at speeds up to 16 m/s. Both light sources are typically placed behind a diffusing translucent paper sheet and can be strobed and synchronized with the camera. When operating in continuous mode (for the Phlox light in the experiments in Sect. 3.1) the exposure time of the system is 42 μs , the minimum allowed exposure time of the camera. In strobed mode, the exposure time is set by the light pulse duration and can be adjusted for each experimental setup: 25 μs in the artificial seawater experiment (Sect. 3.2), 10 μs in the breaking wind-forced waves experiment (Sect. 3.3).

- A telecentric lens (Opto-E TC4MHR096-E, magnification $M = 0.186$, depth of field 39 mm) illuminated by either of the light sources described above. The main advantage of the telecentric lens is the ability to preserve the magnification across the measurement volume. It operates at a fixed working distance of 27.9 cm and has a numerical aperture of $\text{NA} = 0.030$.
- A Basler acA5472-19um camera, with a 5496 x 3672 pixels sensor and a physical pixel size of 2.4 μm . The spatial resolution is obtained by dividing the magnifica-

tion of the telecentric lens, $M = 0.186$, with the pixel size and is 12.9 μm for all experiments presented in this paper. Because of the use of a telecentric lens the spatial resolution is nearly constant across the depth of field.

2.2.2 Droplet detection and size measurement

Once images are acquired, they are analyzed following a 2-step process. First, objects that appear darker than the background, which are presumably droplets, are detected and located using an algorithm applied directly on the recorded image. Then sub-images (with typical size 256 by 256 pixels) are cropped around the detected objects for the second processing step. In the second step the sub-images are analyzed by an algorithm that decides if each detected droplet is in focus, in which case the droplet radius and location are measured. If a droplet is out of focus or a duplicate detection it is removed from the data set. These 2 steps are discussed in detail in the following paragraphs and are illustrated in Fig. 5. Note that images (a) to (c) in Fig. 5 show the minimum intensity map generated by taking the minimum intensity at each pixel location from a total of 1,000 images. The minimum intensity map is used as an example to show the droplet detection and measurement algorithm. However, the processing steps outline below are conducted

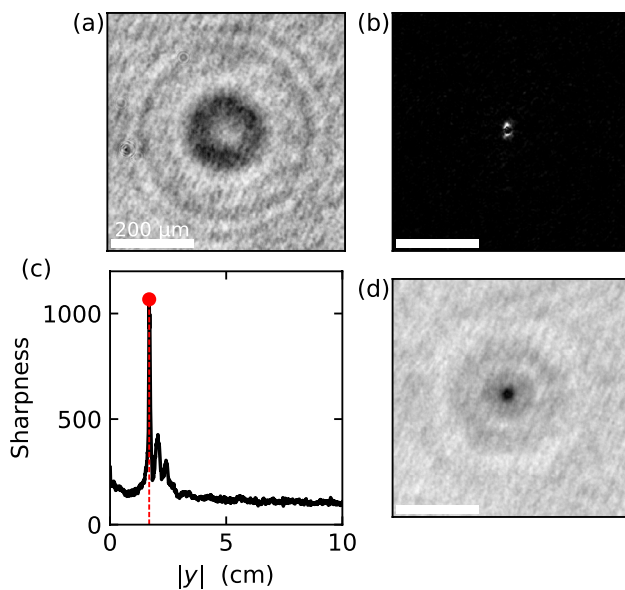


Fig. 3 A sequence of images showing four key image processing steps necessary to find the plane of best focus for a sample droplet with $r \approx 14 \mu\text{m}$. The cropped recorded hologram of the droplet is shown in (a). A spatial map of the droplet sharpness close to the plane of best focus is shown in (b). Note, the image in (b) is artificially enhanced to show the droplet sharpness. The mean droplet sharpness vs. distance from the focal plane ($|y|$) is shown in (c) with a maximum sharpness near the plane of best focus and shown by the red dot and red vertical dashed line, when $|y| \approx 1.69 \text{ cm}$. The definition of sharpness is explained in the text of Sect. 2.1.2. Subplot (d) shows the hologram in (a) reconstructed at the plane of best focus, $|y| \approx 1.69 \text{ cm}$, where the droplet appears sharp and in focus

on individual images, which have a lower density of droplets per image, ranging from 0.02 to 0.50 droplets per image for the experiments presented in this paper. Because of the low droplet density, the process described above allows for a significant size reduction of the data set, typically reducing the data set size by 99 % (see Table 2), with no loss of original information since the extracted sub-images are smaller in size than the original recorded image.

Step 1: droplet detection The first processing step is to compute a background image, taken as the average of 50 to 100 images equally spaced in time from the start to the end of the run under study. The background intensity is normalized for each recorded image, see Fig. 5a and b for an example of the difference between the recorded image (a) and the background normalized image (b). The function `peak_local_max` from the Python package ‘scikit-image’ is used to detect all features that appear darker than the background, the results of this detection are shown as red crosses in Fig. 5b. More details on ‘scikit-image’ can be found in van der Walt et al. (2014). The `peak_local_max` input parameters are deliberately chosen for each data set in order to maximize the detection of all potential droplets. The input parameter values used for the data presented in this article

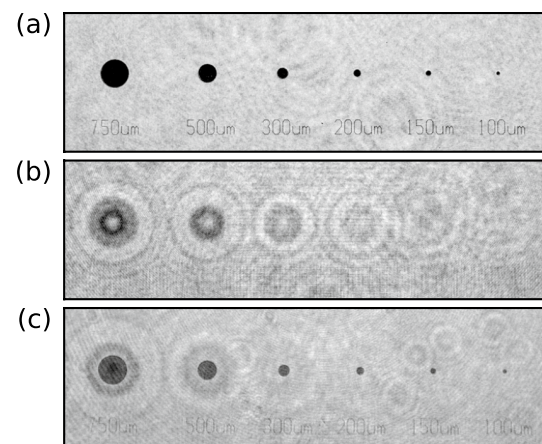


Fig. 4 Images of the reticle used to calibrate the holographic system. The reticle consists of 14 chrome sputter deposited circles ranging in size from $r = 1500$ to $15 \mu\text{m}$. Only six circles ranging from $r = 375$ to $50 \mu\text{m}$ are shown in the image sequence above. Note the number directly below each circle is the diameter in μm . Image (a) shows the calibration target at the focal plane of the lens and recorded using the in-line holographic system. Image (b) shows the same calibration target recorded at the far sidewall of the wave tank used in Erinin et al. (2019) and Erinin et al. (2023) (562 mm away from the focal plane); the interference patterns are produced by the circles on the reticle in image (a). Image (c) is the digital reconstruction of image (b) at $y = 562 \text{ mm}$. Note that the original image is 2560×1600 pixels in size and that the $d = 100 \mu\text{m}$ dot (sixth dot from the left in the bottom row) is visible and in focus in the reconstructed hologram

are the following: the minimal distance separating two intensity peaks, 120 px (or 1.5 mm); the threshold on the peak darkness, 35 (out of 256 levels of intensity); the maximal number of peaks per image, 330. Any duplicate detection of droplets, some of which can be seen on the bottom right corner in Fig. 5b, are discarded at the next processing step. Finally, the recorded image is cropped around the detected peaks of intensity, with a given width of typically 256 px, and the sub-images are stored for analysis in the next processing step.

Step 2: determination of in focus droplets and measurement of radius The second step in the image processing algorithm is to identify in focus droplets and their location and radius. Figure 6a to d shows an example of the image processing steps necessary to achieve this. The procedure operates on each sub-image obtained from the first step, and relies on a Canny edge detection algorithm (referred to as the Canny filter from here on), as implemented in the ‘scikit-image’ Python package. The Canny filter operates on the intensity gradient and is capable of outlining sharp edges in an image, which is used to filter out blurry background objects like out of focus drops. Figure 6a shows an in focus droplet whose boundary was successfully detected by the Canny filter and is shown in red. The detected boundary is used to create a black and white image, see Fig. 6b and the radius of droplet is taken to be the area-equivalent radius of

the white region, r . Figure 6c and d shows an example of an image obtained when the algorithm is applied to the out of focus image of a droplet. This droplet is discarded from the data set because the Canny filter did not detect a boundary.

2.2.3 Depth of field calibration and droplet error estimate

With the shadow imaging technique, the depth of field, δ , depends on the size of the drop, r (Kashdan et al. 2003; Zhou et al. 2020a). The relationship between the depth of field and radius, $\delta(r)$, is quantified by the use of a calibration target made of 14 chrome sputter deposited dots with radius ranging from 15 to 1500 μm (the same target used to calibrate the holographic system, see Sect. 2.1.3). The calibration target is imaged ± 35 mm away from the focal plane in steps of 1 mm, a total of 71 images. Then, the drop detection algorithm is applied on all images (*i.e.* for all dots and at all depth locations), with the same input parameters that are used to process the experimental images.

The depth of field $\delta(r)$ is computed from the calibration target images as a function of the dot radius r , as the difference between the two extreme positions, on either side of the focal plane, where each dot is last detected. We recall that sufficiently far away from the focal plane, a drop or dot appears blurry and the Canny filter is no longer capable of detecting it, as shown in Sect. 2.2.2. The depth of field as a function of dot radius, $\delta(r)$, is shown in Fig. 6e. For dots with a radius $r \geq 250$ μm , the depth of field is nearly constant, $\delta_{r > 250} \approx 39$ mm. For dots with $r < 250$ μm , the depth of field decreases to a value of $\delta = 12$ mm for $r = 50$ μm , the smallest dot detected on the reticle. A function of the form $\delta = \delta_{\infty}(1 - (r_0/r)^{\alpha})$ is manually fitted to $\delta(r)$, where $\delta_{\infty} = 39$ mm, $r_0 = 38$ μm , and $\alpha = 1.5$ in order to interpolate

over the whole range of detected sizes. It should be noted that the cutoff value $r_0 = 38$ μm corresponds to a droplet diameter of 6 pixels in the present setup, which is taken to be the smallest detected droplet radius. As a consequence, the size-dependent depth of field has a direct influence on the measurement volume $V = WH\delta$, with W, H respectively the width and height of the field of view, constant. This method for determining the depth of field as a function of droplet radius is similar to the method described in Tavakolinejad (2010).

The measurement of the calibration target dot radius at various distances from the focal plane is used to estimate the droplet size measurement error E_d in a similar way as done in Sect. 2.1.3 for holography: $E_d = 100 \times \max_y |r(y) - r_i|/r_i$, where $r(y)$ are the radii measured at various distances y within the depth of field, for each calibrated dot radius r_i . Figure 7 shows the relative error E_d for in-line holography and shadow imaging. For large droplets with radii ranging from $r = 625$ to 1500 μm , the error is nearly the same in both techniques and E_d does not exceed 1%. For $r \leq 625$ μm the error in the shadow method increases as droplet diameter decreases, and peaks around $E_d = 4.5\%$ for $r_i = 50$ μm , the smallest measured reticle dot. In the holographic case, the error for droplets with radii between 15 and 625 μm is no more than $E_d \approx 1\%$.

2.3 Droplet radius distributions normalization

One method of comparing the shadow and holographic techniques is by the droplet radius distribution, $N(r)$. Therefore, it is necessary to describe the normalization processes for $N(r)$ between the two methods. The quantity $N(r)$ is reported per unit volume per bin size: $\text{cm}^{-3} \mu\text{m}^{-1}$, where $N(r)dr$ is the

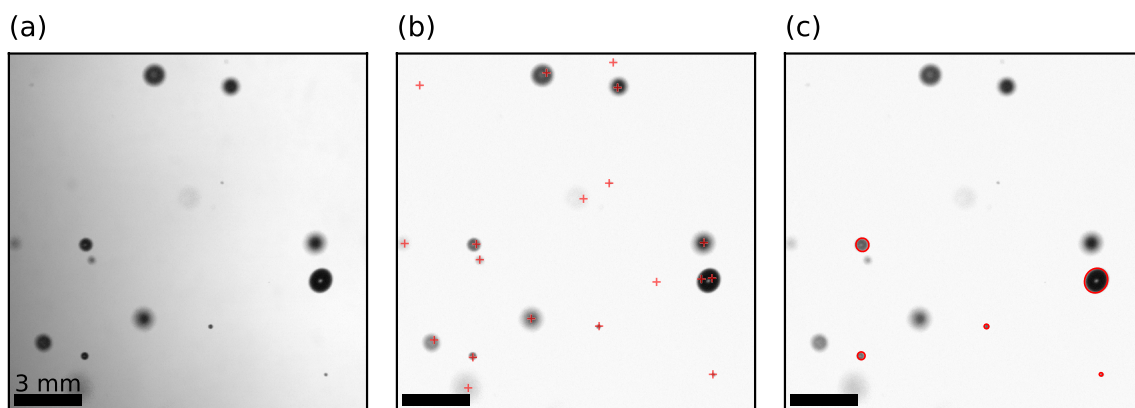


Fig. 5 Image processing for the shadow imaging technique. (a) Intensity minimum of 1,000 stacked raw images. Note that the sequence minimum is shown here for demonstrative purposes only, since the density of droplets is very low on individual images. (b) Potential droplet detection (red pluses), detected from and overlaid on top of the background subtracted image. Intensity minima (*i.e.* poten-

tial drops) are located approximately thanks to the fast algorithm `find_local_maxima` (scikit-image). Drops out of focus and duplicates are handled at the next step. (c) Droplet size and location measurement, using a Canny filter-based detection algorithm and operating on sub-images. The droplet radius measurement is shown in detail in Fig. 6

number of drops with radius between r and $r + dr$, per unit volume. The droplet count in each bin radius is normalized by the total number of recorded images, n_{im} , the depth of field, in the case of shadow imaging $\delta(r)$, and the field of view HW , and is given by:

$$N(r)dr = \frac{\mathcal{N}(r)}{n_{im}HW\delta(r)}, \tag{1}$$

where $\mathcal{N}(r)$ is the count of droplets in the radius bin. Integrating $N(r)$ over a range of sizes yields the total droplet number density in cm^{-3} . In order to draw a direct comparison between holography and shadow imaging $N(r)$ is integrated for all droplets with radius larger than $50 \mu\text{m}$:

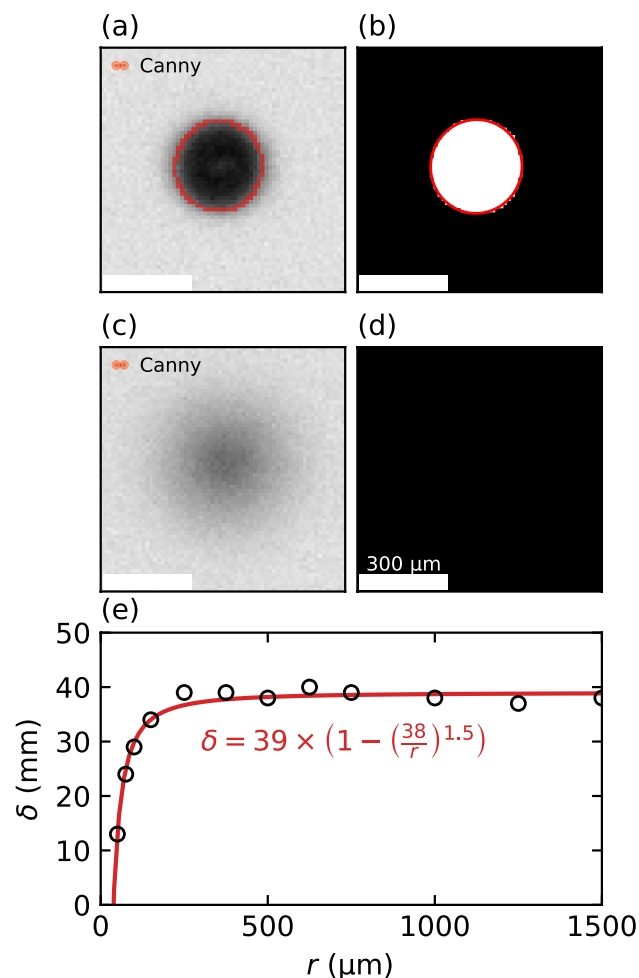


Fig. 6 Detection of in focus droplets, droplet radius measurements, and depth of field correction for shadow imaging. The detection of an in focus droplet from a background subtracted image and the resulting binary image are shown in (a) and (b), respectively. The detected edge from the Canny filter is shown in red in both images and the droplet has a radius of $r = 156 \mu\text{m}$ ($= 12.1 \text{ px}$). An example of an out of focus droplet whose edge boundary was not detected by the Canny filter is shown in (c) and (a). Calibration curve of the depth of field, δ , as a function of the droplet radius r is shown in (e)

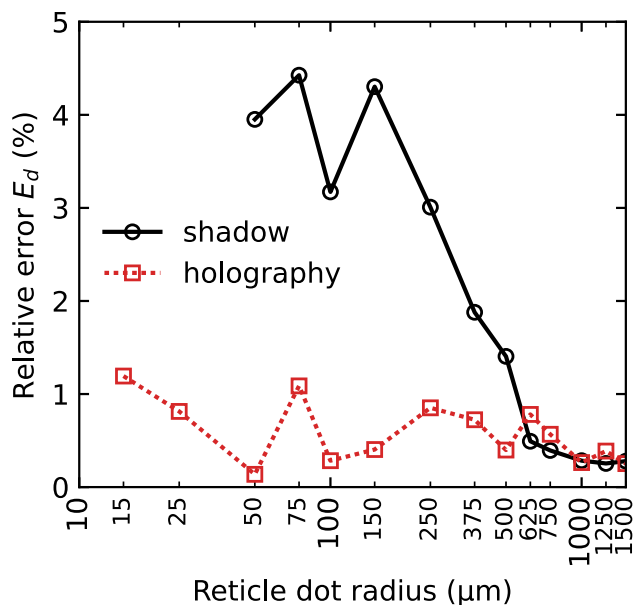


Fig. 7 Error estimate on radius measurement E_d as a function of the dot radius r , for shadow imaging (solid black line) and in-line holography (dotted red line). See Sect. 2.1.3 and 2.2.3 for the shadow and holography definitions of E_d

$$\mathcal{P}_{r>50} = \int_{r>50} N(r)dr = \sum_{r>50} N(r_i)dr_i. \tag{2}$$

The total volume of droplets can be obtained by integrating $N(r)$ and multiplying it by the density of water, $\rho_w = 1000 \text{ kg/m}^3$ and the droplet volume $V = \frac{4\pi}{3}r^3$. The total volume of the droplets is compared between the two cases for $r > 50 \mu\text{m}$ and is given by $\mathcal{V}_{r>50}$.

$$\mathcal{V}_{r>50} = \frac{4\pi\rho_w}{3} \int_{r>50} r^3N(r)dr = \frac{4\pi\rho_w}{3} \sum_{r>50} r_i^3N(r_i)dr_i. \tag{3}$$

The metrics $\mathcal{P}_{r>50}$ and $\mathcal{V}_{r>50}$ are used in Sect. 3.4 as a way to further compare the two methods.

2.4 Holography and shadow imaging data processing times

The processing times for holography and shadow measurements are discussed in this section. The average processing time for the holography depends on the concentration of droplets in each image and is reported in Table 2 for the three experiments. Holographic images are processed on a GPU-compatible MATLAB code on TigerGPU, a high performance computer managed by Princeton Research Computing. TigerGPU includes an Intel Broadwell 2.4 GHz E5-2680 CPUs equipped with NVIDIA P100 GPUs with 16 GB of VRAM and using 4 GB of computer memory. Through the use of multiple nodes in parallel, it is possible

to process 20 runs simultaneously. In the shadow imaging case, only a small fraction of the data is stored and analyzed after the initial data collection and processing step (the original data set size is indicate in parenthesis in Table 2), a reduction of at least 99% of the original data set. The shadow imaging technique requires fewer computing resources and it is possible to compute the full data set on a standard desktop computer (with a 16-thread Intel Xeon W-2145 processor and 32 GB of memory).

2.5 Dry aerosols measurement

In an effort to measure droplets smaller than what the shadow and holographic measurements are capable of, a scanning mobility particle sizer (SMPS) and optical particle sizer (OPS) from TSI, inc. are used. The SMPS is used to measure the dry aerosols generated (with $0.1 \lesssim r \lesssim 1 \mu\text{m}$) in the experiments reported in Sect. 3.2 and is commonly used in the atmospheric aerosol community, see Prather et al. (2013); Wang et al. (2017); Jiang et al. (2022). The present SMPS configuration consists of the following elements: advanced aerosol neutralizer, Model 3088; electrostatic classifier, Model 3082; differential mobility analyzer, Model 3081; condensation particle counter, Model 3752. The OPS measures aerosols (with $0.15 \lesssim r \lesssim 5 \mu\text{m}$) by sampling the air above the bubbling tank, drying the particles, illuminating the aerosol particle in the viewing volume, and relating the properties of the scattered laser light to the particle size by performing an onboard Mie scattering calculation. A refractive index of $1.5 - 0i$ is specified for the measurement of dry sea salt particles using the 660 nm laser of the OPS (Shettle and Fenn 1979). Because the SMPS and OPS measure the diameter of dry aerosols, it is necessary to adjust the radius distributions in order to directly compare them to the wet droplet radius obtained from the holographic and shadow measurements. The dry droplet diameter, D_p , has a direct relationship to the wet droplet radius at production, r , which depends on the salt content in the water ρ_s . Since ρ_s is known in the experiments reported in Sect. 3.2, the wet and dry droplet radii are related by $\frac{4}{3}\pi\rho_s r^3 = \frac{\pi}{6}\rho_{dry} D_p^3$, where ρ_{dry} is the density of the dried salt particle. The relation can be solved for r , resulting in:

$$r = \frac{D_p}{2} \left(\frac{\rho_{dry}}{\rho_s} \right)^{1/3} \tag{4}$$

In artificial seawater ($\rho_s = 36.0 \text{ g L}^{-1}$ and $\rho_{dry} = 2,056 \text{ g L}^{-1}$) a factor of 3.85 is calculated for the conversion between wet and dry aerosols, which is close to the factor 4 reported in Lewis and Schwartz (2004). It should be noted that lower concentrations of salt increase the conversion factor.

The SMPS software outputs size distributions in the following convention, $dN/d \log_{10} D_p$, in cm^{-3} , which is the convention typically used in the aerosol community to report

the aerosol size distributions (Prather et al. 2013; Wang et al. 2017; Jiang et al. 2022). In order to draw a direct comparison between the shadow and holographic measurements, the dry aerosol data have to be represented as $N(r)$ in $\text{cm}^{-3} \mu\text{m}^{-1}$. This is done by using the relation (Lewis and Schwartz 2004):

$$N(r) = \frac{dN}{dr} = \frac{1}{r} \frac{dN}{d \log r} = \frac{1}{r} \frac{dN}{d \log D_p} = \frac{1}{r \log 10} \frac{dN}{d \log_{10} D_p} \tag{5}$$

3 Case comparisons

The optical configurations for holography and shadow imaging were deployed and run simultaneously on three different experiments where droplets are produced. We measured droplet number and radius and use those measurements to calculate the droplet radius distributions. The droplet radius distributions are normalized and used to directly compare holography and shadow imaging. An additional point of comparison is done through the calculation of $\mathcal{D}_{r>50}$ and $\mathcal{V}_{r>50}$. These two metrics offer a direct comparison of the two techniques over their common droplet radius measurement and are discussed in more detail in Sect. 3.4.

3.1 Droplets produced by bursting bubbles in the presence of surfactants

The first set of experiments is performed in a transparent acrylic tank with dimensions $60 \times 60 \times 50 \text{ cm}^3$. The experimental setup is discussed in detail in Néel and Deike (2021) and only a brief overview is given here. Bubbles are produced by blowing dust-free air through 48 needles (inner diameter $305 \mu\text{m}$) located on the bottom of the tank and arranged in a ring pattern. The bubbles produced by the needles are measured using a camera positioned just above the needles (and below the water surface) and are found to be nearly homogeneous in size with $R_b = 1.4 \pm 0.1 \text{ mm}$. As the bubbles rise to the free surface they burst and generate droplets. The droplets are simultaneously measured by the shadow imaging and holographic techniques. Both measurement systems are focused at the center of the tank width and positioned a few centimeters above the still water level.

Anionic surfactant sodium dodecyl sulfate (SDS) is added to the water in various concentrations, c , as a way to modify the water-air interfacial rheology, which changes the surface bubble dynamics dramatically. When the SDS concentration is below the so-called coalescence transition, c_* ($c_* = 8 \mu\text{M}$ for SDS, Néel and Deike (2021)), surface bubbles can merge into larger bubbles which

eventually burst. Above the transition $c > c_*$, bubbles can not merge and their population closely mirrors the bulk bubble radius distribution. It should be noted that the bubbles in the bulk rarely interact as they rise to the surface because they are sparsely populated, even as surfactant concentration is changed. The main focus of the present work is to compare the holographic and shadow imaging techniques in this particular experimental setup.

Figure 8 shows the droplet size distribution for two SDS concentrations, c : below the transition concentration $c = 0.6 \mu\text{M} < c_*$ (red lines) and above it $c = 100 \mu\text{M} > c_*$ (black lines), using in-line holography (dotted lines) and shadow imaging (solid lines). The vertical solid and dotted lines represent the minimum accepted droplet radius, for shadow imaging and holography respectively. The radius size distributions agree well between the two measurement techniques and for the two surfactant concentrations. In the $c = 0.6 \mu\text{M}$ case, both distributions of $N(r)$ reach a local maximum at $r \approx 250 \mu\text{m}$, followed by a local minimum at $r \approx 110 \mu\text{m}$, and continue to increase for $N(r < 110 \mu\text{m})$. Similarly, in the $c = 100 \mu\text{M}$ case both distributions have similar shapes and a change in slope is observed at $r \approx 120 \mu\text{m}$.

3.2 Droplets produced by bursting bubbles in artificial seawater

An acrylic bubbling tank, similar to the one discussed in Sect. 3.1, is used to study the effects of artificial seawater (ASTM D1141-98, Lake Products Company LLC) at two different salt concentrations. The acrylic tank has dimensions $47 \times 47 \times 61 \text{ cm}^3$ and is filled with 35 cm of artificial seawater. A total of 32 needles are arranged in a square pattern on the bottom of the tank with a total of 8 needles per side. Two pumps are completely submerged in the water and placed 6 cm above the needle tips (a depth of 28 cm) at opposite corners of the tank facing each other. When the pumps are turned on they agitate the water in the bulk, breaking apart bubbles in the bulk, changing surface bubble dynamics, and modifying the distribution of droplets produced by the surface bubbles. Droplet data are reported for the pumps “on” condition with a salt concentration of 3.5 and 35 g/kg. The holographic system is configured to image small droplets, and as a result the $r_{\min} = 10 \mu\text{m}$ for the holographic system and the measurement volume of the holographic system is about ≈ 20 percent that of the shadow system. See Table 2 for more details.

Because dry sea salt aerosols play an important role in seawater sprays, dry sea salt aerosols are simultaneously measured using a scanning mobility particle sizer (SMPS, see Sect. 2.5 for more details). In order to conduct the dry aerosol measurements, the air space above the water surface is closed and replaced with the same dust-free air used to

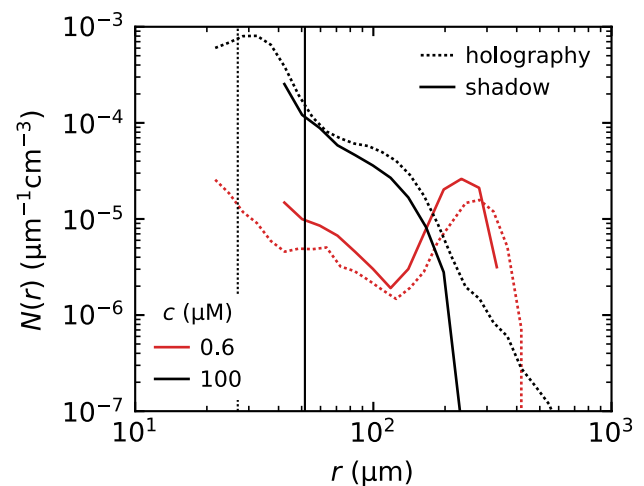


Fig. 8 Droplet radius distributions for bursting bubbles in surfactant-contaminated water using holography (dotted lines) and shadow imaging (solid lines). The vertical lines indicate a radius cutoff at 4 pixels, r_{\min} , where $r_{\min} = 50 \mu\text{m}$ for shadow imaging and $r_{\min} = 27 \mu\text{m}$ for holography. SDS concentrations $c = 0.6, 100 \mu\text{M}$ are shown in red and black lines respectively

generated the bubbles. The humidity and air temperature are monitored inside the chamber throughout the duration of the experiment, where the humidity typically ranges between 70 to 90 percent. Four scans are acquired for each experimental run in the SMPS representation $dN/d \log_{10} D_p$, which are transformed to the $N(r)$ representation by using Equations (4) and (5) and averaged over the multiple scans. Only scans with a minimum of 100 particles are counted.

Figure 9 compares droplet size distributions between the holography (dotted lines), shadow imaging (solid lines), and liquid aerosol measurements from the OPS and SMPS (dashed-dotted and dashed lines, respectively). Two seawater concentrations are reported $\rho_s = [3.6, 36] \text{ g/L}$, with pumps on (green then red for increasing ρ_s). These two concentrations correspond respectively to 10 % and 100 % of the concentration of synthetic seawater, or to salinity values of $[3.5, 35] \text{ g/kg}$. The distributions agree between the shadow and holographic methods. The OPS and SMPS measurements, shown on the left part of Fig. 9, overlap for droplets with $r \approx 1 \mu\text{m}$. The full range of droplet size distributions from the SMPS, OPS, Holography, and Shadow imaging cover approximately four orders of magnitude and appear continuous over the full radius range.

3.3 Droplets produced by breaking wind-forced waves

The final set of experiments are performed at the University of Delaware’s Air-Sea Interaction Laboratory wind-wave facility which is 42 m long, 1 m wide, and 1.25 m tall and is filled with chlorinated tap water to a depth of 0.71 m. Water waves

are continuously generated by a combination of mechanical forcing, from a vertically oscillating wedge located on one end of the tank, and wind forcing from a closed loop wind tunnel. More details on the experimental facility is available in Buckley et al. (2020) and Erinin et al. (2022). Experiments reported in this section are performed with two mechanical wave forcing central frequencies at $f_0 = 1.2$ and 1.8 Hz, with side frequencies at $f_0 \pm 0.05$ Hz, and at a wind speeds of $U_0 = 9.0$ and 9.5 , respectively. At these wind speeds, droplets are nearly continuously generated by the breaking wave field. Droplet measurements are conducted using the holographic and shadow imaging techniques. The in-line holography is located at a fetch of 23.3 m, 16.3 cm above the mean water level while the shadow imaging is located at a fetch of 23.2 m, 17.5 cm above the mean water level. In this configuration, the measurement volume of the holography is ≈ 43 percent larger than the shadow imaging and is capable of measuring droplets down to $r_{\min} = 14 \mu\text{m}$ compared to $r_{\min} = 50 \mu\text{m}$ for shadow imaging, see Table 2.

Figure 10 shows a comparison of droplet size distribution produced by two different wave forcing central frequencies, $f_0 = 1.2$ Hz (in red) and $f_0 = 1.8$ Hz (in black). The vertical solid and dashed lines indicate the minimum accepted droplet radius, r_{\min} , see Table 2 for more details. The slopes and shapes of the distributions of $N(r)$ agree well between the two

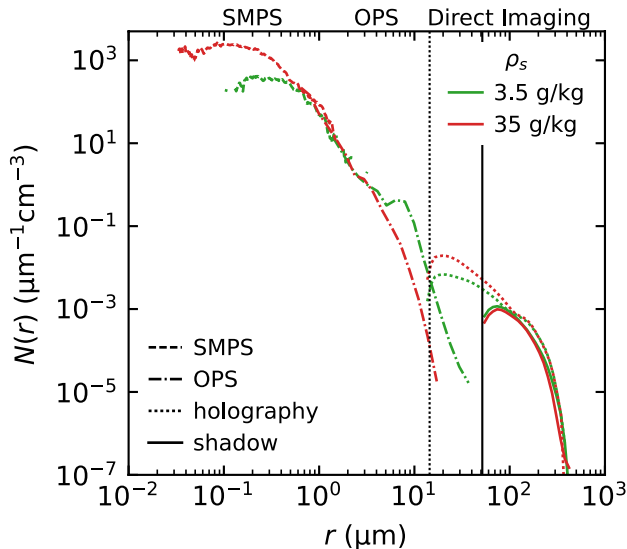


Fig. 9 Droplet radius distributions for bursting bubbles in seawater water using holography (dotted lines), shadow imaging (solid lines), and dry aerosol measurements (dashed lines). For each seawater concentration $\rho_s = [3.6, 36] \text{ g L}^{-1}$, submerged water pumps are used to agitate the bulk water. The vertical lines indicate a radius cutoff, r_{\min} , reported for the two measurement techniques in Table 1. Dry aerosols with radii ranging from $\approx 0.07 - 2 \mu\text{m}$ are measured using a scanning mobility particle sizer (SMPS). The dry-to-liquid conversion factor $r/D_p = \frac{1}{2}(\rho_{\text{dry}}/\rho_s)^{1/3} \approx [4.0, 1.9]$ is applied to convert the aerosol distributions

methods. The distributions from the two methods cover a droplet size range which varies by more than an order of magnitude and increases in $N(r)$ by more than three orders of magnitude, where the two methods are in very close agreement.

3.4 Comparison of average number and volume of droplets per experiment

In order to qualitatively compare the holographic and shadow imaging techniques the droplet density, $\mathcal{P}_{r>50}$, and droplet volume, $\mathcal{V}_{r>50}$, are calculated by integrating Equations 2 and 3 for $r \geq 50 \mu\text{m}$. The droplet density represents the total number of droplets measured with $r \geq 50 \mu\text{m}$ per image, per m^3 and the droplet volume represents the total volume of droplets per image, per m^3 .

Figure 11a and (b) show $\mathcal{P}_{r>50}$ and $\mathcal{V}_{r>50}$, respectively, plotted for the holographic data versus the shadow imaging data for each of the experimental conditions presented in Sect. 8 to 10. The experiments represented in Fig. 11 showcase a wide range of experimental setups, which produce different droplet generating conditions and droplet densities, as well as a variety of experimental setups for the holographic system, ranging from magnifications from 1X to 2X. The diagonal black line has a slope of 1. The data shown in Fig. 11a lies close to that line which means the droplet number correlates well between the two measurement techniques and both techniques are able to measure the droplet size distributions robustly, over their common measurement range. The comparison of the total volume of droplets, $\mathcal{V}_{r>50}$, in Fig. 11b shows that for low droplet volumes, the holographic technique measures a larger total volume of droplets. This effect may be related to the ability of the holographic system to detect larger droplets when compared to shadow imaging, see for example Fig. 8.

4 Comparison of techniques & conclusion

In this paper the experimental techniques in-line holography and shadow imaging are used to measure droplets generated in three experiments. The three experiments are chosen so that a large range of droplet densities are explored, covering nearly three orders of magnitude. The first measurement technique, in-line holography, uses a laser to produce holograms of droplets, which are recorded by a camera and digitally reconstructed at the droplet plane of best focus, after which the droplet radius can be measured accurately. The second method is shadow imaging, where droplets are imaged using a telecentric lens and back-lit by a LED panel. Using image processing techniques, the in focus droplets are detected and their radii are measured while out of focus droplets are discarded. The two methods are found to agree well over their common measurement range and over a large

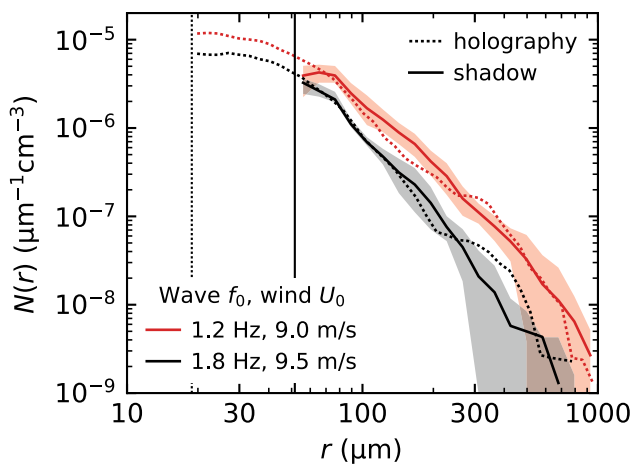


Fig. 10 Droplet radius distributions of droplets produced by mechanically and wind forced breaking waves measured using in-line holography (dotted lines) and shadow imaging (solid lines). Waves are forced with a central frequency of $f_0 = 1.2$ (red lines) and 1.8 Hz (black lines) and the wind speed 36 cm above the still water level ranges from $U_0 = 9.0$ to 9.5 m/s. The shaded areas for the shadow imaging represent the standard deviation on the different runs for each case ($f_0 = 1.2$ Hz: 3 runs, $f_0 = 1.8$ Hz: 4 runs). The vertical lines indicate the radius cutoff, r_{min} , reported for the two measurement techniques in Table 1

range of droplet densities (Sect. 3.4). The advantages and disadvantages of each measurement technique are discussed in the following paragraphs.

The advantages to in-line holography are the greater spatial resolution, larger depth of field, and the high repetition rate and short pulse duration of the laser. Through the use of a microscope objective, the holographic system is

able to measure droplets with radius down to $r = 14 \mu\text{m}$ at a magnification of 2X. Another advantage for the holographic system is the large depth of field, which can be advantageous in low droplet density and transient experiments, like the transient breaking waves reported in Erinin et al. (2019), which used a similar holographic measurement technique. An additional advantage to holography is the high-repetition rate (up to 50 kHz) and short pulse duration, $\mathcal{O}(10 \text{ ns})$, of the laser. The main drawbacks of the holographic technique are the more complicated optical setup (used to produce the collimated laser beam), image processing codes, which are required to find the location and focal point of droplets, the computational resources required to process the holographic images. It should be noted that the holographic optical setup can be made simpler by using a collimated laser diode and a bare camera sensor. These changes would likely result in some technical drawbacks like a diminished depth of field, no control in the spatial resolution, and longer image exposure times when compared to the present configuration. The computational resources used to process the holograms in the present study are significantly larger than those for shadow imaging.

The main advantages to the shadow technique are that it uses a simpler experimental setup and image processing algorithm. The data processing algorithm uses many pre-built functions and algorithms that are easily available on open source platforms like Python. The data can be processed on a desktop workstation in much faster times than the holographic data (see Table 2). The major drawbacks for the current configuration are the fixed working distance and magnification of the telecentric lens, the required calibration process to find the diameter dependent

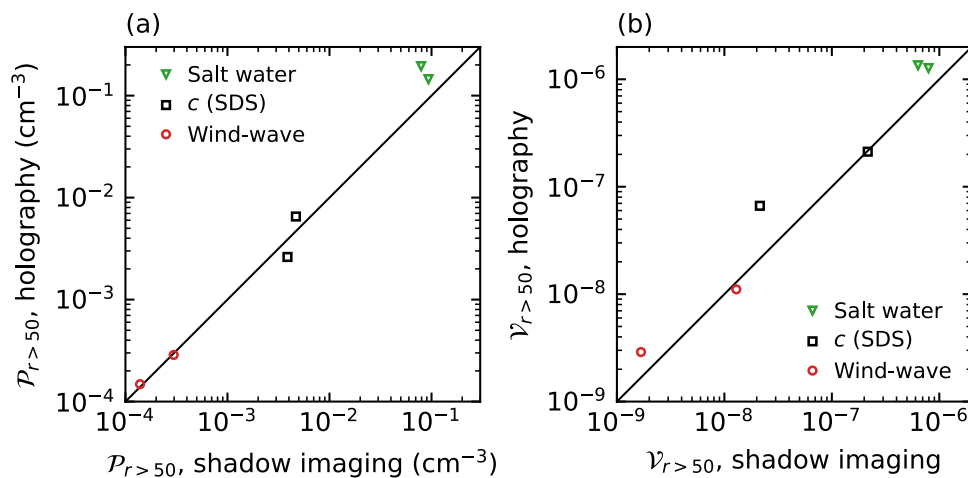


Fig. 11 Droplet density $\mathcal{P}_{r>50}$ (Equation 2), the total number of droplets measured and the total droplet volume $\mathcal{V}_{r>50}$ (Equation 3), calculated for drops with $r \geq 50 \mu\text{m}$ per image, per m^3 plotted for the holographic data versus the shadow data for each of the experimental conditions presented in Sects. 3.1 to 3.3. The diagonal black line has a slope of 1. The black squares show the droplet density from the

‘bursting bubbles in the presence of surfactants’ experiments presented in Sect. 3.1. The green triangles are from the ‘bursting bubbles in artificial seawater’ experiments presented in Sect. 3.2. Finally, the red circles are from the ‘droplets produced by breaking wind-forced waves’ experiments in Sect. 3.3

depth of field for all droplet sizes, and the smaller depth of field, which can make specific types of measurements, like droplet tracking, more difficult. It should be noted that the depth of field for the shadow technique can be augmented using more sophisticated optical setups and processing algorithms, see Zhou et al. (2020a) as an example of such a method. However, in this paper, we showed that a simple shadow imaging technique is capable of producing droplet number and size statistics when compared to a more sophisticated holographic setup.

In this paper, we performed experiments in large and dynamically evolving physical systems that try to reproduce conditions that may be present at much larger scales. We show that both shadow imaging and holography are able to produce reliable droplet number and size measurements in three different experimental setups which cover a large range of droplet densities that span 3 orders of magnitude, including experiments with relatively sparse droplet concentrations as low as 0.02 droplets per image. The experimental setups and image processing steps used for each technique are explained in detail. The droplet radius measurement error for each technique is estimated using a calibration target and it is shown that the radius error is lower for the holographic technique for droplets with $r \leq 625 \mu\text{m}$. The droplet measurements from the three experiments are used to directly compare the two methods. We show that both methods are capable of providing reliable measurement of droplet number and radii, $N(r)$, for radii as low as $r = 14 \mu\text{m}$ using holography and $r \geq 50 \mu\text{m}$ for shadowgraphs. Droplet number, $\mathcal{P}_{r>50}$, and total droplet volume, $\mathcal{V}_{r>50}$, are compared for all droplets with $r \geq 50 \mu\text{m}$. In Sect. 3.2 we provide simultaneous measurements of droplets ($r \geq 14 \mu\text{m}$, using holography) and liquid aerosols ($0.07 \leq r \leq 2 \mu\text{m}$, using an SMPS and $0.15 \lesssim r \lesssim 5 \mu\text{m}$ using an OPS), the first such measurements to the best of our knowledge. We show that the two techniques can robustly measure the droplet number and size over a large range of droplet densities ranging from $\mathcal{P}_{r>50}$, ranging from $10^{-4} \leq \mathcal{P}_{r>50} \leq 10^{-1} \text{cm}^{-3}$. Using the direct comparison of the two techniques, the advantage for shadow imaging technique is shown to be the simplicity of the setup and processing and the main advantage to in-line holography is the greater range of applicability.

Supplementary Information The online version contains supplementary material available at <https://doi.org/10.1007/s00348-023-03633-8>.

Author's contributions MAE, BN, MM, JHD, LD designed and performed the research, MAE, BN, and MM analyzed the data. MAE, BN, LD wrote the paper. MAE wrote the code to process holographic images while working on his dissertation at the University of Maryland. BN wrote the shadow image processing and calibration algorithm while a postdoctoral scholar at Princeton. All authors edited the paper.

Funding The support of the Division of Ocean Sciences of the National Science Foundation under grant OCE1849762 to LD and OCE1925060 to JHD are gratefully acknowledged. This work was also supported by the Metropolis Initiative at Princeton University. This material is based upon work supported by the National Science Foundation Graduate Research Fellowship awarded to MM. The authors would like to acknowledge the Princeton Research Computing resources at Princeton University which is consortium of groups led by the Princeton Institute for Computational Science and Engineering (PICSciE) and Office of Information Technology's Research Computing. The authors also acknowledge Prof. Joseph Katz for allowing us to use his GPU-compatible hologram reconstruction algorithm.

Data availability The data that support the findings of this study are available from the corresponding author, LD, upon reasonable request.

Declarations

Conflict of interest The authors declare that they have no financial or personal competing interests.

Ethical approval Not applicable.

Open Access This article is licensed under a Creative Commons Attribution 4.0 International License, which permits use, sharing, adaptation, distribution and reproduction in any medium or format, as long as you give appropriate credit to the original author(s) and the source, provide a link to the Creative Commons licence, and indicate if changes were made. The images or other third party material in this article are included in the article's Creative Commons licence, unless indicated otherwise in a credit line to the material. If material is not included in the article's Creative Commons licence and your intended use is not permitted by statutory regulation or exceeds the permitted use, you will need to obtain permission directly from the copyright holder. To view a copy of this licence, visit <http://creativecommons.org/licenses/by/4.0/>.

References

- Ade SS, Kirar PK, Chandrala LD, Sahu KC (2023) Droplet size distribution in a swirl airstream using in-line holography technique. *J Fluid Mech* 954:A39
- Baker L, DiBenedetto M (2023) Large-scale particle shadow tracking and orientation measurement with collimated light. *Exp Fluids* 64(3):52
- Barnkob R, Rossi M (2020) General defocusing particle tracking: fundamentals and uncertainty assessment. *Exp Fluids* 61(4):1–14
- Beyersdorf P (2014) Laboratory optics: a practical guide to working in an optics lab. Peter Beyersdorf
- Bongiovanni C, Chevaillier JP, Fabre J (1997) Sizing of bubbles by incoherent imaging: defocus bias. *Exp Fluids* 23(3):209–216
- Bongiovanni C, Dominguez A, Chevaillier J-P (2000) Understanding images of bubbles. *Eur J Phys* 21(6):561
- Boulesteix S (2010) Cisaillement d'une interface gaz-liquide en conduite et entraînement de gouttelettes [Shearing of a gas-liquid interface in a pipe and droplet entrainment]. PhD thesis, l'Université Paul Sabatier
- Buckley MP, Veron F, Yousefi K (2020) Surface viscous stress over wind-driven waves with intermittent airflow separation. *J Fluid Mech* 905:A31
- de Leeuw G, Andreas EL, Anguelova MD, Fairall CW, Lewis ER, O'Dowd C, Schulz M, Schwartz SE (2011) Production flux of sea spray aerosol. *Rev Geophys* 49(2)

- Deike L, Reichl B, Paulot F (2022) A mechanistic sea spray generation function based on the sea state and the physics of bubble bursting. *AGU Adv* 3(6):2022AV000750
- Erinin M, Néel B, Ruth D, Mazzatenta M, Jaquette R, Veron F, Deike L (2022) Speed and acceleration of droplets generated by breaking wind-forced waves. *Geophys Res Lett*, p e2022GL098426
- Erinin MA (2020) The Dynamics of Plunging Breakers and the Generation of Spray Droplets. PhD thesis, University of Maryland, College Park
- Erinin MA, Wang SD, Liu R, Towle D, Liu X, Duncan JH (2019) Spray generation by a plunging breaker. *Geophys Res Lett* 46(14):8244–8251
- Erinin MA, Wang SD, Liu X, Liu C, Duncan JH (under review, 2023). Plunging breakers - part 2. droplet generation. *J Fluid Mech*
- Geißler P, Jähne B (1995) Measurements of bubble size distributions with an optical technique based on depth from focus. In: *Proc Int Symp Air Water Gas Transfer*, pp 351–362
- Guildenbecher DR, Engvall L, Gao J, Grasser TW, Reu PL, Chen J (2014) Digital in-line holography to quantify secondary droplets from the impact of a single drop on a thin film. *Exp Fluids* 55:1–9
- Guildenbecher DR, Gao J, Chen J, Sojka PE (2017) Characterization of drop aerodynamic fragmentation in the bag and sheet-thinning regimes by crossed-beam, two-view, digital in-line holography. *Int J Multiphase Flow* 94:107–122
- Guildenbecher DR, Gao J, Reu PL, Chen J (2013) Digital holography simulations and experiments to quantify the accuracy of 3d particle location and 2d sizing using a proposed hybrid method. *Appl Opt* 52(16):3790–3801
- Hayashi J, Watanabe H, Kurose R, Akamatsu F (2011) Effects of fuel droplet size on soot formation in spray flames formed in a laminar counterflow. *Combust Flame* 158(12):2559–2568
- Jiang X, Rotily L, Villermaux E, Wang X (2022) Submicron drops from flapping bursting bubbles. *Proc Nat Acad Sci* 119(1):e2112924119
- Kamiya T, Asahara M, Yada T, Mizuno K, Miyasaka T (2022) Study on characteristics of fragment size distribution generated via droplet breakup by high-speed gas flow. *Phys Fluids* 34:012118
- Kashdan JT, Shrimpton JS, Whybrew A (2003) Two-phase flow characterization by automated digital image analysis. part 1: fundamental principles and calibration of the technique. *Parti Part Syst Char Measure Description Part Prop Behav Powders Other Disperse Syst* 20(6):387–397
- Katz J, Sheng J (2010) Applications of holography in fluid mechanics and particle dynamics. *Ann Rev Fluid Mech* 42:531–555
- Khanam T, Rahman MN, Rajendran A, Kariwala V, Asundi AK (2011) Accurate size measurement of needle-shaped particles using digital holography. *Chem Eng Sci* 66(12):2699–2706
- Lewis ER, Schwartz SE (2004) *Sea Salt Aerosol Production: Mechanisms, Methods, Measurements and Models-A Critical Review*. Number 152 in *Geophysical Monograph*. Am Geophys Union, Washington, D.C
- Li C, Miller J, Wang J, Koley S, Katz J (2017) Size distribution and dispersion of droplets generated by impingement of breaking waves on oil slicks. *J Geophys Res Oceans* 122(10):7938–7957
- Ling H, Katz J (2014) Separating twin images and locating the center of a microparticle in dense suspensions using correlations among reconstructed fields of two parallel holograms. *Appl Opt* 53(27):G1–G11
- Machicoane N, Aliseda A, Volk R, Bourgoin M (2019) A simplified and versatile calibration method for multi-camera optical systems in 3d particle imaging. *Rev Sci Instruments* 90(3):035112
- McEwan I, Sheen T, Cunningham G, Allen A (2000) Estimating the size composition of sediment surfaces through image analysis. In: *Proceedings of the institution of civil engineers-water and maritime engineering*, vol 142, pp 189–195. Thomas Telford Ltd.
- Néel B, Deike L (2021) Collective bursting of free-surface bubbles, and the role of surface contamination. *J Fluid Mech* 917
- Néel B, Deike L (2022) Velocity and size quantification of drops in single and collective bursting bubbles experiments. *Phys Rev Fluids* 7(10):103603
- Néel B, Erinin MA, Deike L (2022) Role of contamination in optimal Droplet production by collective bubble bursting. *Geophys Res Lett* 49(1):e2021GL096740
- Pan G, Meng H (2003) Digital holography of particle fields: reconstruction by use of complex amplitude. *App Opt* 42(5):827–833
- Poelma C (2020) Measurement in opaque flows: a review of measurement techniques for dispersed multiphase flows. *Acta Mech* 231(6):2089–2111
- Prather KA, Bertram TH, Grassian VH, Deane GB, Stokes MD, DeMott PJ, Aluwihare LI, Palenik BP, Azam F, Seinfeld JH et al. (2013) Bringing the ocean into the laboratory to probe the chemical complexity of sea spray aerosol. *Proc Nat Acad Sci* 110(19):7550–7555
- Ramírez de la Torre RGG, Jensen A (2023) Sizing of particles and droplets using 3d-ptv, an openptv post-processing tool. *Measure Sci Technol*
- Ruth DJ, Néel B, Erinin MA, Mazzatenta M, Jaquette R, Veron F, Deike L (2022) Three-dimensional measurements of air entrainment and enhanced bubble transport during wave breaking. *Geophys Res Lett* 49(16):e2022GL099436
- Sanchis A, Johnson GW, Jensen A (2011) The formation of hydrodynamic slugs by the interaction of waves in gas-liquid two-phase pipe flow. *Int J Multiphase Flow* 37(4):358–368
- Schnars U, Falldorf C, Watson J, Jüptner W (2015) Digital holography. In: *Digital holography and wavefront sensing*, pp 39–68. Springer
- Settles GS (2001) *Schlieren and shadowgraph techniques*. Springer, Berlin
- Shettle E, Fenn R (1979) Models for the aerosols of the lower atmosphere and the effects of humidity variations on their optical properties. Technical Report AFGL-TR-79-0214, Optical Physics Division, U.S. Air Force Geophysics Laboratory
- Soontaranon S, Widjaja J, Asakura T (2008) Extraction of object position from in-line holograms by using single wavelet coefficient. *Opt Commun* 281(6):1461–1467
- Tavakolinejad M (2010) Air bubble entrainment by breaking bow waves simulated by a 2D+ T technique. University of Maryland, College Park
- Troitskaya Y, Kandaurov A, Ermakova O, Kozlov D, Sergeev D, Zilitinkevich S (2018) The “bag breakup” spume droplet generation mechanism at high winds. part i: Spray generation function. *J Phys Oceanogr* 48(9):2167–2188
- Tropea C (2011) Optical particle characterization in flows. *Annu Rev Fluid Mech* 43:399–426
- Van de Hulst H, Wang R (1991) Glare points. *Appl Opt* 30(33):4755–4763
- van der Walt S, Schönberger JL, Nunez-Iglesias J, Boulogne F, Warner JD, Yager N, Gouillart E, Yu T, the scikit-image contributors, (2014) Scikit-image: image processing in Python. *Peer J* 2:e453
- Veron F (2015) Ocean Spray. *Annu Rev Fluid Mech* 47:507–538
- Veron F, Hopkins C, Harrison E, Mueller J (2012) Sea spray spume droplet production in high wind speeds. *Geophys Res Lett* 39(16)
- Wang X, Deane GB, Moore KA, Ryder OS, Stokes MD, Beall CM, Collins DB, Santander MV, Burrows SM, Sultana CM et al. (2017) The role of jet and film drops in controlling the mixing state of submicron sea spray aerosol particles. *Proc Nat Acad Sci* 114(27):6978–6983
- Warncke K, Geppert S, Sauer B, Sadiki A, Janicka J, Koch R, Bauer H-J (2017) Experimental and numerical investigation of the primary breakup of an airblasted liquid sheet. *Int J Multiphase Flow* 91:208–224

- Zhou W, Tropea C, Chen B, Zhang Y, Luo X, Cai X (2020) Spray drop measurements using depth from defocus. *Measure Sci Technol* 31:075901
- Zhou W, Tropea C, Chen B, Zhang Y, Luo X, Cai X (2020) Spray drop measurements using depth from defocus. *Measure Sci Technol* 31(7):075901

Publisher's Note Springer Nature remains neutral with regard to jurisdictional claims in published maps and institutional affiliations.